Near-field laser-induced fluorescence velocimetry of neutral xenon in a 6-kW Hall thruster plume

IEPC-2007-229

Presented at the 30th International Electric Propulsion Conference, Florence, Italy
September 17-20, 2007

Timothy B. Smith*, Wensheng Huang†, Bryan M. Reid ‡,
and
Alec D. Gallimore§
Plasmadynamics and Electric Propulsion Laboratory,
University of Michigan, Ann Arbor, MI 48105, USA

We present laser-induced fluorescence (LIF) measurements of neutral xenon ($6s\ ^2[3/2]^0_2$) in the near-field plume of a 6-kW Hall thruster. The 823.163 nm (air) beam from a TUI Optics TA-100/830 tapered-amplifier diode laser is focused along an axial beamline onto a submillimeter interrogation volume, from which we collect resonant LIF. Polarization control via a rotating half-wave plate keeps the input beam polarization parallel to the magnetic field, minimizing distortion of the LIF spectrum by Zeeman splitting in regions of high magnetic field intensity. Doppler velocimetry of LIF spectra taken at the discharge channel exit returns bulk axial velocities at discharge voltages of 53 to 300 V and mass flow rates of 5 through 17.5 mg/s.

I. Introduction

Considerable effort is being invested into understanding the role of neutral flow dynamics in the operation of conventional Hall thrusters. In particular, understanding the near-field neutral velocity will provide insight into the effects of anode injection schemes, wall accommodation, and resonant charge-exchange collisions in the near-field plume. A comprehensive review of past neutral flow dynamics research indicates that anode injection schemes can significantly affect thruster efficiency, lifetime, stability, and thermal margin.[1] In response to these potential benefits, the neutral flow dynamics in the discharge channel are being altered to maximize propellant utilization by increasing the neutral flow uniformity and residence time. By optimizing the neutral flow dynamics in the discharge channel, the operational envelope of Hall thrusters can be expanded to high specific impulse and high thrust-to- power. At these challenging operational regimes, the importance of propellant utilization and thruster stability are amplified.

To track the effects of changes in neutral flow dynamics, neutral properties will be tracked in the very-near-field (< 1 thruster diameter). Measuring the neutral component of partially ionized plasmas is relatively difficult with electrostatic probes; however, non-intrusive optical methods are well suited for this application. This experiment uses Laser-Induced Fluorescence (LIF) velocimetry of neutral xenon on a planar interrogation region extending downstream of the discharge channel exit. Correlation of the velocity profile with analytical models, plume simulations, and electrostatic probe measure will permit a thorough investigation of the effects of neutral flow non-uniformity and residence time.

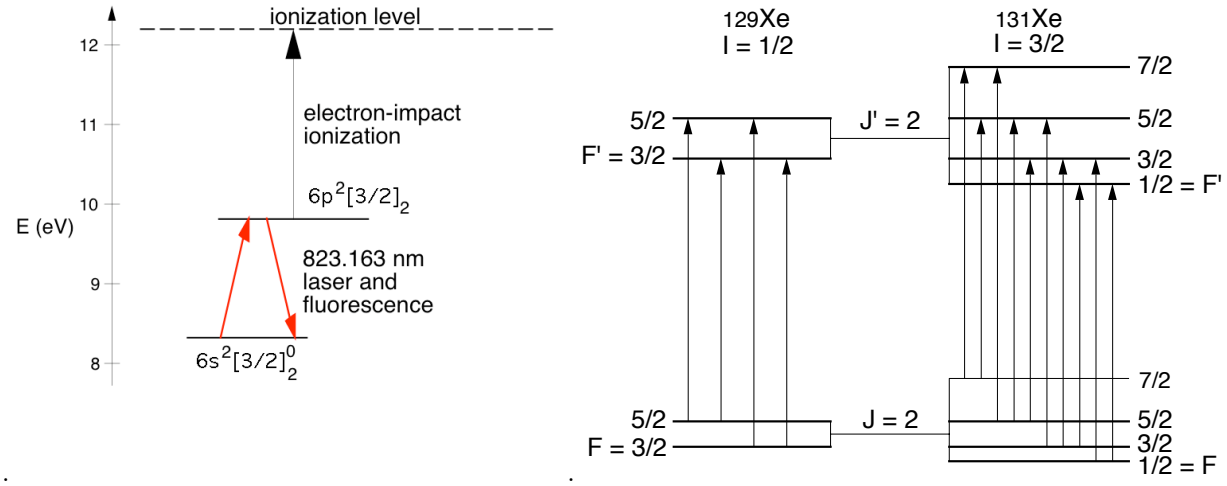

(a) Fine structure.

(b) Hyperfine structure for absorption line.

Figure 1. Optogalvanic and LIF schemes using Xe I absorption at 823. nm.

II. Theory

Figure 1(a) shows the fine structure transitions for optogalvanic and resonant LIF spectroscopy of the 823.163 nm (air) transition of Xe I. Absorption of 823.163 nm laser light causes xenon atoms resting in the metastable lower state $6s\ ^2[3/2]_2^0$ to jump to the excited upper state $6p\ ^2[3/2]_2$. Since this upper state is closer to the first ionization potential for xenon (12.1298 eV) than the lower state, the probability of electron-impact ionization (and thus the galvatron discharge current) increases linearly with the upper state population, providing an optogalvanic signal. Those atoms which are not ionized out of the upper state quickly decay; since there are no other allowed transitions from the $6p\ ^2[3/2]_2$, the $6p\ ^2[3/2]_2 \rightarrow 6s\ ^2[3/2]_2^0$ fluorescence at 823.163 nm provides a strong, but resonant LIF signal.

A. Doppler shift and broadening

Consider a light source with vacuum wavelength λ and frequency $\nu = c/\lambda$. An observer who is stationary with respect to the light source will see light at the same frequency ν. An observer moving towards the light source will see a bluer (*i.e.*, higher-frequency) light than the stationary viewer, while an observer moving away from the light source will see a redder (*i.e.*, lower-frequency) light.

In LIF, this Doppler effect appears as a shift in the resonant frequency ν_0 as the laser is scanned over a very short frequency range. The change in photon frequency $\triangle\nu = \nu - \nu_0$ for a particle with velocity $\mathbf{v}$ passing through a light beam of wave vector $\mathbf{k}$ is

$$\triangle\nu = -\frac{\mathbf{k}\cdot\mathbf{v}}{2\pi}. \tag{1}$$

Given a beamwise velocity component $v_k \equiv \mathbf{v}\cdot\hat{\mathbf{k}}$, Eqn. 1 gives the beamwise velocity-to-frequency transformations

$$\nu = \left(1 - \frac{v_k}{c}\right)\nu_0 \tag{2}$$

$$v_k = \left(1 - \frac{\nu}{\nu_0}\right)c. \tag{3}$$

A swarm of particles with a normalized velocity distribution $f(\mathbf{v})$ will also "see" the frequency of incoming photons shifted by the relative velocity of the particle in the direction of the photon. The resulting Doppler

*Research Fellow and Lecturer, Aerospace Engineering, timsmith@umich.edu
†Graduate Research Assistant, Aerospace Engineering, davhuang@umich.edu
‡Graduate Research Assistant, Aerospace Engineering, reidb@umich.edu
§Professor and Associate Dean, Aerospace Engineering, rasta@umich.edu

lineshape will be shifted by the beamwise bulk velocity $u_k = \langle \mathbf{v} \cdot \hat{\mathbf{k}} \rangle$ and broadened by the thermal width of the beamwise distribution $f(v_k)$. The generalized Doppler lineshape $d(\nu)$, when properly normalized so that

$$\int_{-\infty}^{\infty} d(\nu)\, d\nu = 1, \tag{4}$$

is given by

$$d(\nu) = \frac{c}{\nu_0} f\left(\left[1 - \frac{\nu}{\nu_0}\right] c\right). \tag{5}$$

In species with no hyperfine structure (HFS), the LIF spectrum $i(\nu)$ is the convolution of the Doppler broadening with the natural (or lifetime) broadening function

$$l(\nu) = \frac{\triangle\nu_n}{2\pi} \frac{1}{(\nu - \nu_0)^2 + (\triangle\nu_n/2)^2} \tag{6}$$

where $\triangle\nu_n = A_j/(2\pi)$ is the natural linewidth for state j. This Lorentzian function is usually much narrower for warm gases than the Doppler broadening. In this case, the natural broadening can be replaced by a Dirac delta function,

$$i(\nu) = d(\nu) \otimes l(\nu) \approx d(\nu) \otimes \delta(\nu) = d(\nu), \tag{7}$$

letting us directly transform the LIF spectrum into an excellent approximation of the beamwise velocity distribution.

B. Hyperfine structure

In xenon (and other species with HFS), the LIF spectrum can be modeled as the convolution of the hyperfine splitting function $h(\nu)$ with natural and Doppler broadening functions,

$$i(\nu) = h(\nu) \otimes l(\nu) \otimes d(\nu). \tag{8}$$

The hyperfine splitting $h(\nu)$ is a series of n Dirac delta functions,

$$h(\nu) = \sum_{j=1}^{n} p_j \delta(\nu - \nu_j). \tag{9}$$

where ν_j is the j^{th} hyperfine line center and p_j is the j^{th} hyperfine line intensity. The $6s\ ^2[1/2]_1^0 \rightarrow 6\ ^2[3/2]_2$ transition of Xe I has $n = 18$ such hyperfine splittings.

Hyperfine structure consists of two components. Isotopic splitting is caused by the mass and nuclear volume differences between isotopes in the sample. Nuclear-spin splitting is caused by the coupling between the nuclear spin $\mathbf{I}$ and the total electronic angular momentum $\mathbf{J}$. For the sake of brevity, we will henceforth use the term "HFS constants" to denote the combined set of isotopic shifts and nuclear-spin interaction constants.

There are nine stable isotopes of xenon, seven of which have natural abundances greater than one percent. Each of these isotopes causes a slightly different transition energy E_{ij}, resulting in isotopic splitting. Table 1 presents naturally-occurring xenon isotopic abundances and shifts (conventionally defined relative to the center frequency for ^{132}Xe).

Table 1. Isotopic abundance and shift relative to ^{132}Xe for the Xe I $6s\ ^2[3/2]_2^0 \rightarrow 6p\ ^2[3/2]_2$ transition at 823.163 nm (air) nm (from Jackson and Coulombe *et al.*[4]). No isotopic shift values are available for ^{124}Xe and ^{126}Xe.

Mass (amu)	124	126	128	129	130	131	132	134	136
Abundance (%)	0.0096	0.009	1.92	26.4	4.1	21.1	26.9	10.4	8.9
Shift (MHz)	—	—	84.1	96.5	37.1	72.8	0.0	-38.9	-116.9

Seven of the nine stable isotopes of xenon have even atomic mass, resulting in no nuclear spin $\mathbf{I}$. The two isotopes with an odd atomic mass, however, have non-zero nuclear spin quantum numbers I. The lighter

isotope, ^{129}Xe, has $I = 1/2$, while ^{131}Xe has $I = 3/2$. These non-zero nuclear spins cause nuclear-spin splitting of the atomic energy levels. This nuclear-spin splitting is 1 to 2 orders of magnitude broader than the isotopic splitting, and provides most of the characteristic shape of our absorption line.

The total angular momentum $\mathbf{F} = \mathbf{I} + \mathbf{J}$ takes quantum number values

$$F = I + J, I + J - 1, \ldots, |I - J| \tag{10}$$

where J is the total electronic angular momentum quantum number.[9] The extra term energy due to nuclear-spin splitting is given by[8]

$$E_{\text{nss}} = A\frac{C}{2} + BD, \tag{11}$$

where A is the nuclear magnetic dipole interaction constant, B is the nuclear electric quadrupole interaction constant, and the terms

$$C = F(F + 1) - I(I + 1) - J(J + 1) \tag{12}$$

and

$$D = \frac{(3C/4)(C + 1) - I(I + 1)J(J + 1)}{2I(2I - 1)J(2J - 1)} \tag{13}$$

contain the nuclear spin-orbit interactions.

Table 2 presents energy levels and nuclear-spin structure constants for the Xe I absorption line at 823.163 nm (air), taken from Jackson and Coulombe.[6]

Table 2. Energy levels and nuclear-spin structure constants for the Xe I $6s\ ^2[1/2]^0_2 \rightarrow 6\ ^2[3/2]_2$ transition at 823.163 nm.

Level	E_i (eV)	A_{129} (MHz)	A_{131} (MHz)	B_{131} (MHz)
$6s\ ^2[3/2]^0_2$	8.353155	−2385	706	253
$6p\ ^2[3/2]_2$	9.8210934	−892	264	30

The transition rule for nuclear-spin splitting is $\triangle F \equiv F - F' = [0, \pm 1]$, where F is the upper and F' is the lower state's total angular momentum quantum number. (The zero-zero transition is forbidden, $F = 0 \not\rightarrow F' = 0$.) Figure 1 shows the fine structure and nuclear-spin splitting for he Xe I $6s\ ^2[1/2]^0_2 \rightarrow 6\ ^2[3/2]_2$ transition at 823.163 nm.

The relative intensity of each nuclear-spin split component is given for a $J \rightarrow J - 1$ transition by[10]

$$I(F \rightarrow F - 1) \propto \frac{P(F)P(F - 1)}{F} \tag{14}$$

$$I(F \rightarrow F) \propto \frac{(2F + 1)}{F(F + 1)}P(F)Q(F) \tag{15}$$

$$I(F - 1 \rightarrow F) \propto \frac{Q(F)Q(F - 1)}{F} \tag{16}$$

where $P(F) = (F + J)(F + J + 1) - I(I + 1)$ and $Q(F) = I(I + 1) - (F - J)(F - J + 1)$.

For the isotopes with even mass numbers (i.e., without nuclear-spin splitting), the line intensity p_j is linearly proportional to the naturally-occurring abundance for each isotope. The line intensities of ^{129}Xe and ^{131}Xe are linearly proportional to the product of the isotopic abundance and the relative intensity of the nuclear-spin split components.

C. Propellant utilization and ionization fraction

Neglecting facility effects, the propellant utilization determines the ionization fraction and neutral number density in the near-field plume of a Hall thruster. Since the Xe I LIF signal strength and signal-to-noise ratio are roughly proportional to the neutral number density, propellant utilization has an undeniable influence on the effectiveness of Xe LIF in the Hall thruster plume.

In most analyses, the propellant utilization is defined as the ratio of ion flux to the total particle flux. For an atomic species with Z electrons, a generalized expression for propellant utilization is

$$\eta_u = \sum_{i=1}^{Z} n_i u_i \Bigg/ \sum_{i=0}^{Z} n_i u_i \tag{17}$$

where n_i is the number density and u_i is the axial velocity for species i (and we define $i = 0$ for neutrals, $i = 1$ for single ions, $i = 2$ for double ions, and so forth). Given the total number density

$$n = n_0 + n_1 + \ldots = \sum_{i=0}^{Z} n_i \tag{18}$$

and defining the ionization fraction

$$\alpha_i = n_i / n \tag{19}$$

for each ionization state $1 \leq i \leq Z$, the generalized propellant utilization can be expressed in terms of ionization fraction as

$$\eta_u = \sum_{i=1}^{Z} \alpha_i u_i \Bigg/ \sum_{i=0}^{Z} \alpha_i u_i \ . \tag{20}$$

When multiple ionization is negligible, the propellant utilization becomes

$$(\eta_u)_1 = \frac{n_1 u_1}{n_0 u_0 + n_1 u_1} \tag{21}$$

or, in terms of the ionization fraction $\alpha_1 = n_1/n$,

$$(\eta_u)_1 = \left[\frac{1 - \alpha_1}{\alpha_1} \left(\frac{u_0}{u_1} \right) + 1 \right]^{-1} . \tag{22}$$

Equation 22 can be rearranged to yield the ionization fraction as a function of propellant utilization, neutral velocity and ion velocity:

$$\alpha_1 = \left[\frac{1 - (\eta_u)_1}{(\eta_u)_1} \left(\frac{u_1}{u_0} \right) + 1 \right]^{-1} . \tag{23}$$

Since $\alpha_0 + \alpha_1 = 1$ for negligible multiple ionization, Equation 23 shows that the neutral number density n_0 (and thus, the LIF signal strength and SNR) varies as

$$n_0 = n \left(1 - \left[\frac{1 - (\eta_u)_1}{(\eta_u)_1} \left(\frac{u_1}{u_0} \right) + 1 \right]^{-1} \right) \tag{24}$$

Thus, the LIF signal intensity (*ceteris paribus*)

- *decreases* with increasing ion velocity u_1, and
- *decreases* with increasing propellant utilization $(\eta_u)_1$.

In the limit of 100% propellant utilization, the ionization fraction goes to 100% and the Xe I LIF signal (and SNR) drop below the threshold of detection.

III. Apparatus and Procedure

A. Facility

Experiments were performed in the Large Vacuum Test Facility (LVTF) at the University of Michigan. The LVTF is a ϕ6 m $\times$9 stainless steel-clad cylindrical chamber. Pumping is provided by seven single-stage CVI model TM-1200 cryopumps and liquid nitrogen shrouds, with a nominal pumping speed of 240,000 l/s. Facility pressure is monitored by two hot-cathode ionization gauges, and base pressure is approximately $1.2\times$

10^{-7} Torr. The facility pressure during thruster operation at 11 mg/s total xenon flow rate is approximately 7.6×10^{-6} Torr, corrected for xenon.

Xe I LIF spectra were recorded at the discharge channel and cathode exit planes of a 6-kW laboratory model Hall thruster. During these experiments, the 6-kW Hall thruster was mounted on two crossed translation tables. The axial translation table has a 1-m range of motion, while the radial translation table has a 2-m travel. Both translation stages are PC-controlled by a custom LabView VI, with locational resolution on the order of 0.1 mm. A vertically-adjustable support structure atop the translation tables elevated the thruster to the chamber centerline, allowing the plume to expand ~ 4 meters along the chamber axis.

Research-grade xenon propellant (99.999% pure) was supplied to the thruster by separate commercially available flow meters and controllers, having an accuracy of $\pm 1\%$ of full scale. Calibration of the flow system by the constant volume method[2] includes the effects of compressibility.[3]

B. Laser and optics

The laser system used in this experiment is a TUI Optics TA-100/830 tapered-amplifier diode laser. This system has a nominal linewidth of ~ 10 MHz, a tuning range of 820 nm to 836 nm, and a mode-hop-free range of over 10 GHz. Though capable of output powers in excess of 500 mW, off-peak efficiency drops and Faraday isolation of the tapered amplifier reduce the available output power at the upper end of the system wavelength range (835 ± 1 nm) to approximately 250 mW.

The master oscillator for this system is an ECDL. Coarse wavelength control is provided by Peltier cooling of the ECDL and micrometer adjustment of the ECDL feedback grating angle. PC control of the fine tuning is provided by a LabVIEW VI, which uses the auxiliary output of a Stanford SR810 lock-in amplifier to send a control voltage to a piezoelectric transducer (PZT) driving the ECDL feedback grating. Feedback circuitry in the ECDL power supply decreases the master oscillator diode current during a PZT sweep to maximize the mode-hop-free range. In order to include the effect of changing laser output power, we normalize our reported LIF and OGS spectra by a quadratic curve-fit to the master oscillator power. It is important to note that this normalization carries an implicit assumption that the absorption line is not saturated. Steering mirrors inside the TA-100 enclosure couple the ECDL output into the tapered amplifier diode, which boosts the ECDL output power by a factor of more than 20 while maintaining the master oscillator wavelength and linewidth.

Although power changes over the course of a frequency scan, simply normalizing the signal by the laser power would give misleading results when the LIF lineshape is highly saturated. Instead, we use an external photodiode to monitor laser power, and take care to keep the central peak of the photodiode signal within a 5% tolerance band for all scans. This allows a basis for comparing the magnitude of the signal between multiple scans at different operating conditions.

Figure 2 shows a schematic of the diode laser table contents. A wedged beam pickoff diverts two beamlets (beams A and B, each ~ 5 mW) from the main TA-100 output beam. The main beam passes through an initial beam splitter, which diverts $\sim 40\%$ of the main beam to a second beam splitter that further dividing the beam into two ~ 50 mW beamlets (beams C and D). The remaining ~ 120 mW of main beam power (beam E) continues on toward the LVTF.

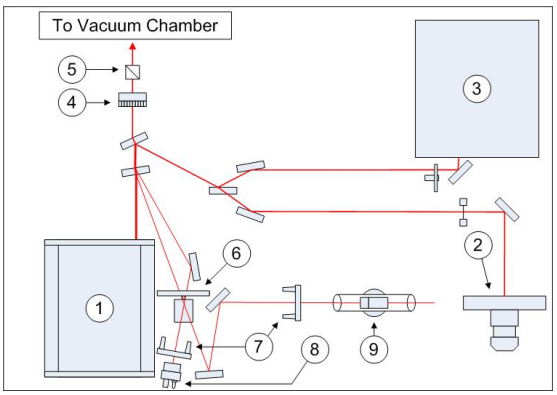

Index:	
1.	Tunable diode laser
2.	2-GHz etalon assy
3.	Wavemeter
4.	Half-wave plate
5.	Polarizing beam cube
6.	Chopper
7.	Neutral density filter
8.	Photodiode
9.	Optogalvanic cell

Figure 2. Optical table schematic for 6-kW Hall thruster LIF experiment.

Beam A goes through a Stanford SR540 chopper running at 1.6 kHz to two mirrors, which steer the beam through a neutral density filter, into a Hamamatsu L2783 galvatron, and terminates at a Thorlab DET110 photodiode. The optogalvanic current and photodiode voltage signals go to Stanford SR810 lock-in amplifiers, yielding optogalvanic and absorption spectra for the galvatron discharge. During saturation studies, a half-wave plate, polarizing beam splitter cube, and a neutral density filter are inserted in the beam path to control the laser power entering the galvatron.

Beam B goes through same SR540 chopper, and passes through a neutral density filter to an external photodiode. Since the photodiode has a known efficiency and is connected to a preamplifier of known characteristics, we can make highly precise measurements of the beam power.

Beam C is steered by two mirrors through a variable neutral density filter to the Burleigh WA-1000 wavemeter. The wavemeter can determine laser wavelength with a 1 pm resolution, which is sufficient for coarse alignment and troubleshooting of the laser. Oversampling of the PZT control voltage permits greater wavelength resolution by a quadratic curve-fit to the wavemeter output, but does not improve the absolute bias of the laser wavelength measurement.

Beam D is directed by two mirrors through an iris into a Burleigh SA-91 etalon assembly with a free spectral range of 2 GHz and a finess of 256. This provides a series of sharp frequency markers, allowing high-resolution ($\sim$ 10 Mz) measurement of the frequency interval swept during a laser scan. Sampling steps were never set this small during this experiment, though; typical sampling intervals ranged between 25 and 50 MHz. Cost and time limitations were the major driver for this reduced frequency resolution, but the need to reduce thermal drift of the etalon spacing was also factor.

Beam E continues on through a half-wave plate, a polarizing cube, and a Stanford SR540 optical chopper running at 1700 kHz before reaching the first of 3 near-infrared mirrors. These mirrors steer the beam through the upper sapphire window, into the LVTF, and onto the input window of the LVTF periscope.

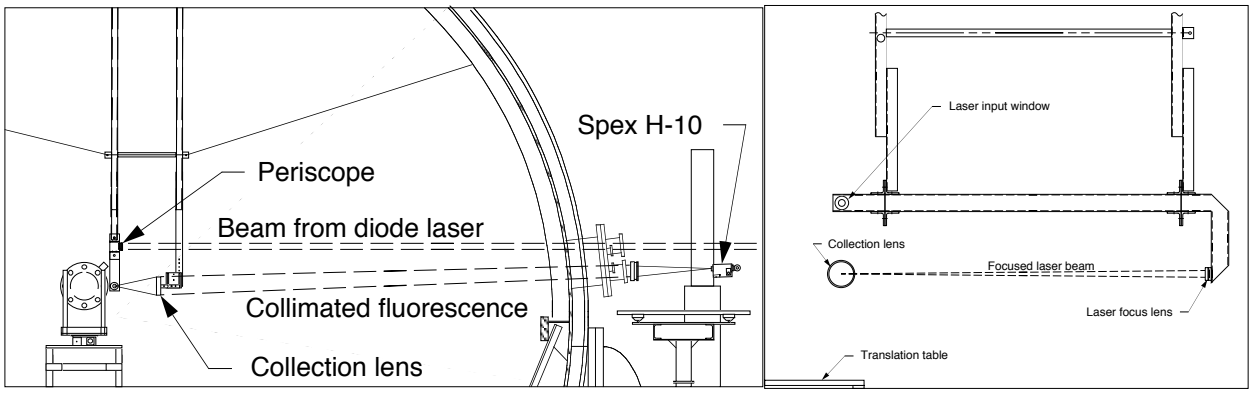

(a) Looking upstream (north). (b) Looking west.

Figure 3. Laser beam delivery and fluorescence collection optics in the LVTF.

Figures 3(a) and 3(b) show the LVTF beam handling setup. Approximately 50 mW of beam power enters the periscope through a replacable antireflection (AR) coated window. Three near-infrared mirrors within the periscope direct the beam to a focusing telescope parallel to the cathode and solenoid axis, reducing the beam diameter to less than 1 mm.

Two separate AR windows protect the ϕ100 mm, $f/2.5$ collection lens. The collimated fluorescence from the thruster plume passes out of the LVTF through another sapphire window and into a ϕ100 mm, $f/5$ lens. Two protected aluminum mirrors direct the focusing beam onto a Spex H-10 monochromator (using 500-μm slits) with a Hamamatsu 928 PMT. A Stanford SR850 lock-in amplifier extracts the LIF signal from the PMT output. The interrogation volume, defined by the intersection of the laser beam and the doubly-magnified monochromator slit image, is a $\phi 1 \times 1$ mm cylinder oriented parallel to the cathode axis.

C. Optogalvanic cell

The optogalvanic cell used in this experiment is a Hamamatsu L2783-42 XeNe-Mo galvatron. The core of the galvatron is a ϕ6.25 mm pair of cylindrical Mo electrodes, centered in a ϕ25 x 120 mm glass cylinder

filled with approximately 3 Torr of xenon and and 4 Torr of neon. The ends of the cylinder are angled approximately 10 degrees from a perpendicular to the electrode axis; though this is less than Brewsters angle for a glass-air interface, it reduces the likelihood of retroreflected beams entering the discharge. This design permits unobstructed passage of a laser beam along the axis shared by the cylinder and electrodes.

A 192 V discharge across the galvatron electrodes produces a reasonably cool, dense, stationary plasma. Additionally, this voltage seems to maximize the population of the $6s\ ^2[3/2]^0_2$ metastable and provide clean optogalvanic signal. A ballast resistor prevents runaway current growth after the discharge is struck, and provides a simple method of measuring the discharge current. The voltage drop across the ballast resistor is connected to a Stanford SR-810 lock-in amplifier through a 3.33 μF, 450 V capacitor. The capacitor passes the AC component of the voltage drop, while isolating the lock-in from high DC voltages.

IV. Results

Our original plan was to take Xe I LIF spectra at the cathode exit and in a region downstream of discharge channel. After taking scans at multiple radial locations across the discharge channel exit, we planned to continue downstream until the metastable lower-state density became too low for good LIF signal-to-noise ratios (SNRs).

Unfortunately, we quickly found that at normal operating conditions for this Hall thruster (discharge voltage $V_d \geq 300V$ and anode mass flow $\dot{m}_A \geq 10$ mg/s), the neutral density was so low that acceptable signal-to-noise ratios (SNR>1) required excessively-long scans ($T \geq 3600$ s). Since Equation 23 implies that the neutral density will tend to increase with decreasing discharge voltage, we decided to carry a survey of discharge voltages below 300 V. In the course of investigating these low-voltage discharges, we discovered that anode mass flow rate also affects the LIF signal quality.

A. Zeeman splitting

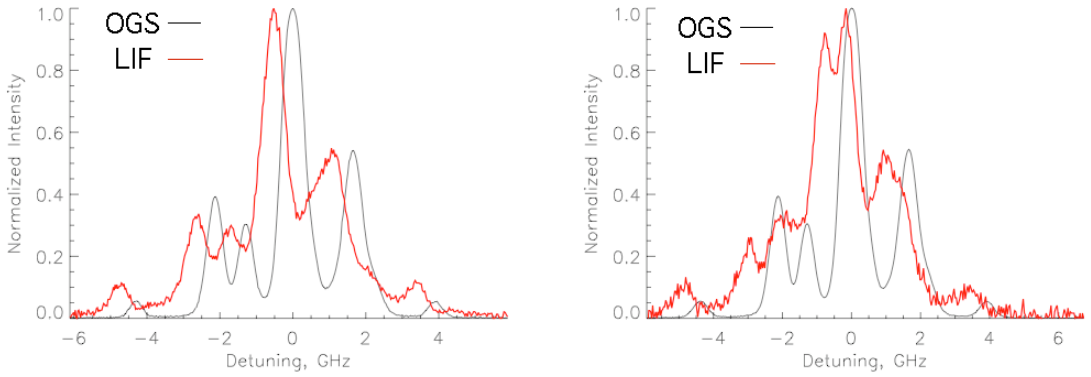

(a) $B = 0$ gauss (b) $B = 174$ gauss

Figure 4. Optogalvanic (black line) and cathode exit plane LIF (red line) spectra at 823.163 nm (air), cathode operating without an anode discharge.

Figures 4(a) and 4(b) show how an axial magnetic field at the cathode exit causes Zeeman splitting of the LIF spectrum at 823.136 nm. The SNR is quite good for both spectra, largely because the discharge current is off. Because the magnetic field has a strong component parallel to the beam vector ($\mathbf{B} \parallel \mathbf{k}$) and the beam vector is always perpendicular to the polarization vector ($mbE \perp \mathbf{k}$), it is impossible in this case to remove Zeeman splitting by rotating the polarization vector into π-polarization.

Figures 5(a) and 5(b) show how increased discharge current adds noise to the cathode LIF spectrum. The Zeeman splitting in Figure 4(b) is difficult to distinguish from noise in Figure 5(a), while the noise in Figure 5(b) completely overwhelms the Zeeman splitting.

Figures 6(a) and 6(b) show how Zeeman splitting in the largely-radial magnetic field at the discharge channel exit can be reduced by rotating the laser polarization vector. Both spectra were recorded at the

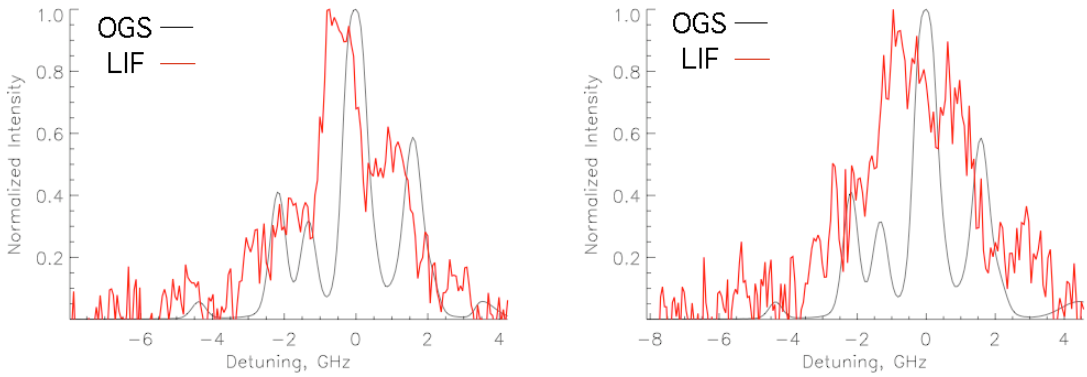

(a) $\dot{m}_A = 5$ mg/s (b) $\dot{m}_A = 15$ mg/s

Figure 5. Optogalvanic (black line) and cathode exit plane LIF (red line) spectra at 823.163 nm (air), thruster operating at 150 V discharge voltage.

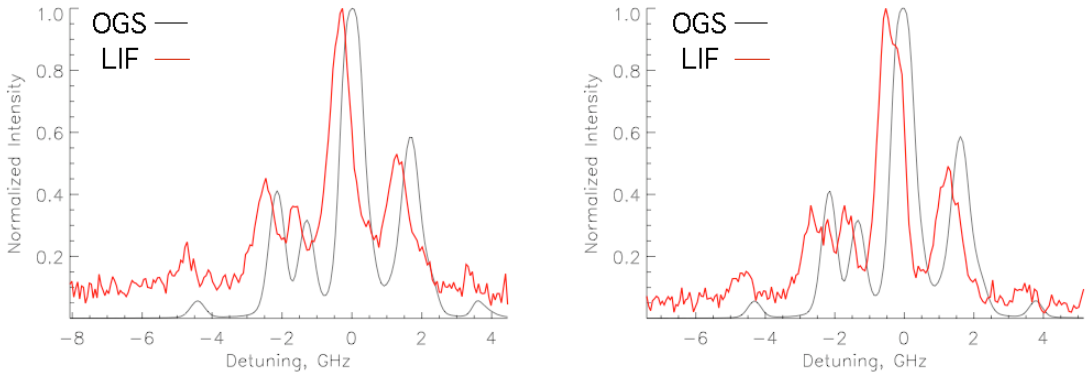

(a) π-polarization (b) σ-polarization

Figure 6. Optogalvanic (black line) and discharge channel exit plane LIF (red line) spectra at 823.163 nm (air), thruster operating at 150 V discharge voltage and $\dot{m}_A = 5$ mg/s.

discharge channel centerline, with the thruster operating at a 150 V discharge and an anode mass flow of 5 mg/s. The inner and outer coil currents were identical for both spectra. The laser polarization in Figure 6(a) was horizontal, so the polarization vector was parallel to the mostly-radial magnetic field ($\mathbf{E} \parallel \mathbf{B}$, or π-polarization) at the interrogation volume. For Figure 6(b), we used the half-wave plate and polarizing cube beamsplitter to rotate the laser polarization so that it was vertical, placing the polarization perpendicular to the magnetic field ($\mathbf{E} \perp \mathbf{B}$, or σ-polarization). The resulting shift is slight, but unmistakeable: the main and secondary peaks shown in Figure 6(a) show definite Zeeman splitting in Figure 6(b).

B. LIF signal strength vs. discharge voltage

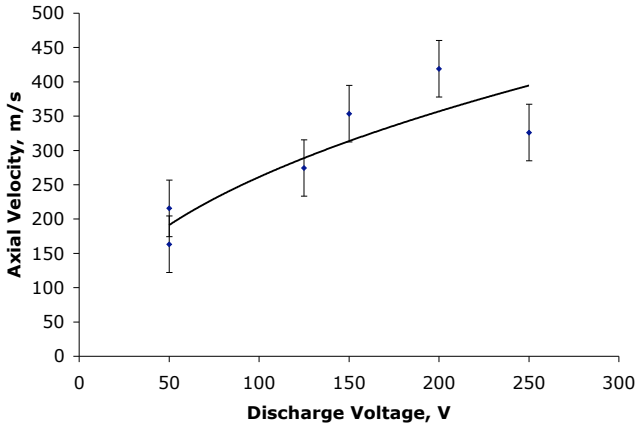

Figure 7. Axial velocity of neutral particles at the discharge chamber exit as a function of discharge voltage for a constant 10 mg/s anode flow rate.

Figure 7 shows the axial bulk velocity of metastable neutrals at the discharge chamber exit as a function of discharge voltage. The ±41.17 m/s error bars correspond to the 50-MHz resolution of the LIF scans. The trendline is proportional to $\sqrt{V_D}$; this is reasonable if we model the neutral flow as an electrothermal thruster, where the exhaust velocity varies as the square root of the stagnation temperature. Since convective losses would scale linearly with discharge velocity for constant discharge current, the stagnation temperature could also be expected to increase linearly with discharge voltage. (Since ion velocity is also proportional to $\sqrt{V_D}$, this behavior might also indicate entrainment.)

Figure 8(a) shows the magnitude of the central peak versus the discharge voltage. The magnitude was found by fitting a quadratic curve to the region in each scan representing the central peak. For a low-noise scan, this region includes all data points above half of the approximate peak value. For high noise scan, this region includes all points that rises above the noise amplitude of the region surrounding the peak. As such, no peak magnitude can be found if no peak is readily identifiable. This is the reason why no 300 V data is included in this figure.

All scans in this survey were done at an anode flow rate of 10 mg/s. In order to save time and cut thermal drift, the relatively noise-free 50-V LIF scans were carried out using an integration time constant $\tau = 1$ s on the lock-in amplifier. The remaining scans were carried out using a $\tau = 3$ s. All other hardware configurations were kept constant throughout these scans. Note that while great care is taken to minimize thermal drift between these scans, a large uncertainty bracket (±25%) is included to show that thermal drifting can be a significant problem in these scans. A trendline has been added to shows that the peak magnitude decreases rapidly as the discharge voltage increased.

In order to compare SNRs for scans taken at varying values of the integration time constant τ, we define

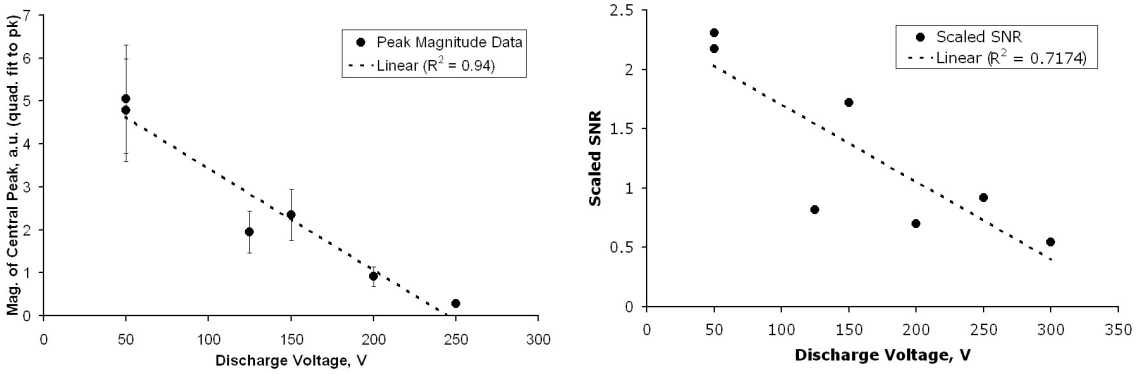

(a) Magnitude (b) SNR

Figure 8. Magnitude and scaled signal-to-noise ratio of neutral LIF signal at the discharge chamber exit as a function of discharge voltage for a constant 10 mg/s anode flow rate.

a scaled SNR

$$R_s = \frac{\sigma_s}{\sigma_n}\sqrt{\frac{\tau}{\tau_0}} \tag{25}$$

where σ_s is the standard deviation of the signal[a], σ_n is the standard deviation of the noise[b], and τ_0 is a scaling time constant (defined as $\tau_0 = 1$ s). The statistical argument behind Equation 25 assumes that the noise is broadband, which is generally true for scans done with time constants that are on the same order of magnitude.

Figure 8(b) shows the scaled SNR as a function of the discharge voltage. A linear curve-fit is included to show the general trend. As the discharge voltage is increased, the signal rapidly gets drowned out by the noise. Uncertainty bracket was not included due to the complexity of defining uncertainty for scaled SNR.

When taken in combination, Figures 8(a) and 8(b) strongly indicate that the number of neutrals in the metastable lower state (presumably proportional to the total number of neutrals at the exit plane) decreases dramatically with increasing discharge voltage. As a result, the LIF signal (proportional to the metastable population) is effectively drowned out by noise (roughly independent of discharge voltage) before the discharge voltage reaches 300 V.

C. LIF signal strength vs. anode mass flow rate

Figure 9 shows the axial bulk velocity of metastable neutrals at the discharge chamber exit as a function of anode mass flow rate. As before, the ±41.17 m/s error bars correspond to the 50-MHz resolution of the LIF scans. The trendline is approximately constant; this is again reasonable if we model the neutral flow as an electrothermal thruster. At constant discharge voltage and increasing mass flow rate, the convective heat loss rate would increase linearly but the stagnation temperature (and thus the bulk velocity) would remain approximately constant.

Figure 10(a) shows the magnitude of the central peak versus the anode mass flowrate at a constant discharge voltage of 150 V. This plot was processed using the same techniques described for Figure8(a). Data for the mass flow rate of 17.5 mg/s was not included in this figure because the peak was difficult to locate. We used a 1-s time constant for the 10 mg/s scan, and 3-s time constants for the remaining scans. Once again, we made every effort to minimize thermal drift during these scans.

Figure 10(b) shows how the scaled SNR varies with anode mass flow rate at a constant discharge voltage of 150 V. As before the SNR calculation and scaling we carried out in the same manner as described for Figure 8(b) .

[a]In the absence of *a priori* knowledge of the signal, we used a 10-point box smoothing of the noisy signal to approximate the noise-free signal.

[b]Noise was defined as the difference between the smoothed signal and the noisy signal.

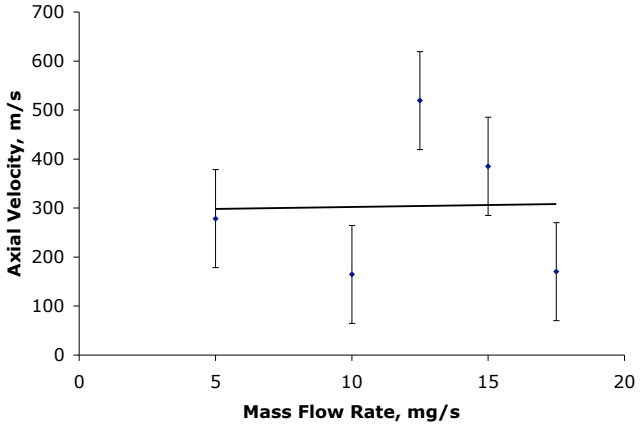

Figure 9. Axial velocity of neutral particles at the discharge chamber exit as a function of anode flow rate for a constant 150 V discharge

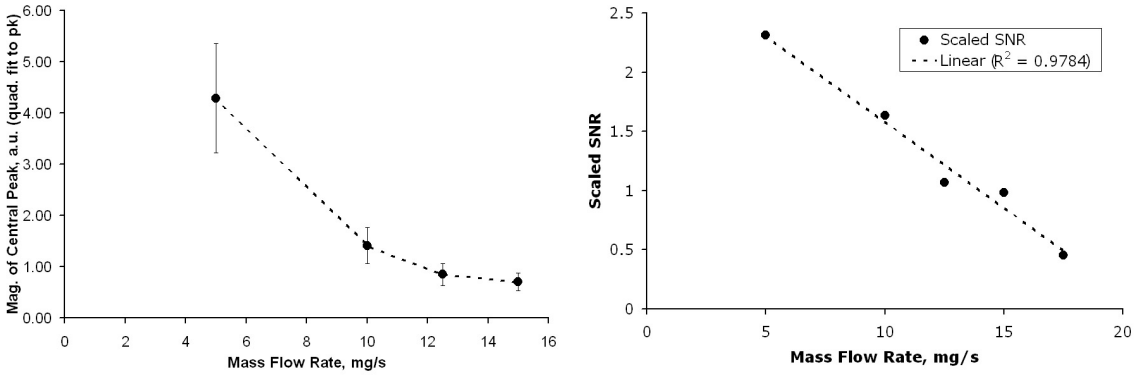

(a) Magnitude

(b) SNR

Figure 10. Magnitude and scaled signal-to-noise ratio of neutral LIF signal at the discharge chamber exit as a function of mass flow rate for a constant 150 V discharge.

When taken in combination, Figures 9, 10(a) and 10(b) show a somewhat counter-intuitive trend: as the anode mass flow rate increases, the neutral velocity remains constant and the number of metastable neutrals decreases. If the metastable population scales with the total neutral population, this implies that the propellant utilization must increase (independant of neutral speed) with mass flow rate.

V. Conclusions

We have carried out LIF scans of the neutral xenon $6s\ ^2[3/2]^0_1$ metastable at the discharge channel of a 6-kW Hall thruster. The neutral velocity tends to rise with the square root of the discharge voltage at constant mass flow rate, but remains essentially independant of mass flow rate at constant discharge voltage; both behaviors indicate that the neutral flow in a Hall thruster follows the same principles found in an electrothermal thruster. Rapidly-deteriorating LIF signal strengths and signal-to-noise ratios indicate that the neutral density decreases monotonically with both discharge voltage and with mass flow rate.

VI. Acknowledgements

This research was supported by the Air Force Office of Scientific Research grants F49620-02-1-0051 and F49620-01-1-0061 (Dr. Mitat Birkan is the contract monitor for both). The authors are greatly appreciative of this support.

We would also like to thank the graduate and undergraduate students at PEPL for their assistance in experimental setup and operation, and the Department's technical support staff for their aid with facility repairs and modifications.

References

[1]Reid, B.M., Gallimore, A.D., and R.R. Hofer, "Review of Hall thruster neutral flow dynamics," *30th International Electric Propulsion Conference,* IEPC-2007-38, September 2007.

[2]Linnell, J.A. and A.D. Gallimore, "Internal plasma potential measurements of a Hall thruster using plasma lens focusing," *41st Joint Propulsion Conference*, AIAA-2005-4402, July 2005.

[3]Dymond, J.H., and E.B. Smith, *The Virial Coefficients of Pure Gases and Mixtures, a Critical Compilation*, Oxford University Press, New York, 1980,

[4]Jackson, D.A. and M.C. Coulombe. "Isotope shifts in the arc spectrum of xenon," *Proceedings of the Royal Society of London A***338**(1974) 277-298.

[5]Suzuki, M., Katoh, K., and N. Nishimiya. "Saturated absorption spectroscopy of Xe using a GaAs semiconductor laser," *Spectrochimica Acta A***58**(2002) 25192531.

[6]Jackson, D.A. and M.C. Coulombe. "Hyperfine structure in the arc spectrum of xenon," *Proceedings of the Royal Society of London A***327**(1972) 137-145.

[7]E. Browne. *Table of Isotopes,* C. M. Lederer and V. S. Shirley, ed. 7th ed., Wiley, 1978.

[8]S. Svanberg. *Atomic and Molecular Spectroscopy: Basic Aspects and Practical Applications.* 3rd ed., Springer-Verlag, 2001.

[9]H. Kopfermann. *Nuclear Moments.* Academic Press, 1958.

[10]C. C. Candler. *Atomic Spectra and the Vector Model.* Van Nostrand, 1964.